Localized west-dipping seismic structure defines the Elgin-Lugoff Swarm Sequence in South Carolina

Oluwaseyifunmi E. Adeboboye[1], Lindsay Y. Chuang[1], Miguel Neves[1,2], Zhigang Peng[1], Dan Frost[3], Steve Jaume'[4]

[1]School of Earth and Atmospheric Sciences, Georgia Institute of Technology, USA
[2]Université Côte d'Azur, IRD, CNRS, OCA, Géoazur, Sophia Antipolis, France
[3]School of the Earth, Ocean, and the Environment College of Arts and Sciences, University of South Carolina, USA
[4]Department of Geology and Environmental Sciences, College of Charleston, USA

Key Points:

- A four-month dense nodal deployment was conducted to record ongoing seismic swarms in Elgin-Lugoff, South Carolina.
- A high-resolution catalog reveals a west-dipping, north-south-striking fault plane conjugate to the East Piedmont Fault System.
- The orientation and scale of the Elgin swarm sequence may suggest a localized stress reactivation by the regional NE-SW compression.

This manuscript is a preprint and has not yet undergone peer review. A version of this manuscript has been submitted to Seismological Research Letters for consideration.

Corresponding author: Oluwaseyifunmi E. Adeboboye, oadeboboye3@gatech.edu

Abstract

An unusual earthquake swarm began in December 2021 between the towns of Elgin and Lugoff in South Carolina, United States. This area is characterized by historically low seismicity, but by April 2024 it has experienced 97 small earthquakes listed in the USGS catalog, presenting a unique opportunity to investigate the dynamics of earthquake swarms in stable continental regions. These events are located in a north-south diffuse trend, cross-cutting the Eastern Piedmont Fault System (EPFS), a Late Paleozoic dextral strike-slip fault, however, the location uncertainties were too large to reveal any obvious structure. Starting from October 2022, we deployed 85 Smartsolo 5-Hz 3-component nodal stations for four months in the direct vicinity of the Elgin swarm. By using a combination of deep learning and match filter techniques (MFT) for event detection, and double-difference relocation methods for precise earthquake locations, we obtain up to 100 high-resolution microearthquake locations, as compared with 4 events listed in the USGS catalog for the deployment period. In our improved catalog, we report significantly smaller magnitudes in comparison to those listed in the USGS catalog, with a local magnitude ranging from -2.17 to 2.54 and achieving a magnitude of completeness at -0.22. The relocated catalog outlined a single fault plane of nearly north-south strike and west-dipping, generally consistent with one of the magnetic anomalies in this region (Shah et al., 2023). We also determine focal mechanisms solutions for selected events in this swarm sequence which shows mainly strike-slip faulting with nodal planes aligning with the north-south striking seismic cluster. Our relocated catalog can be used to constrain the location of other swarm events outside the nodal recording period and provide a robust benchmark dataset for further analysis of the swarm sequence.

1 Introduction

Earthquake swarms are defined as sequences of seismic events closely clustered in space and time, without a single outstanding mainshock (Mogi, 1963). They occur worldwide in regions such as volcanic areas, geothermal regions, or mid-ocean ridges ((Benoit & McNutt, 1996; Fischer et al., 2014; Holtkamp & Brudzinski, 2014) and are thought to be primarily driven by external forces such as fluid migrations (Shelly et al., 2016; Chen et al., 2012; Ross et al., 2019, 2020), aseismic slip (Lohman & McGuire, 2007), or dike propagation in volcanic settings (Hill, 1977; Toda et al., 2002), rather than a cascading stress transfer.

Starting from December 27, 2021, a prolonged intraplate swarm sequence began with a magnitude 3.3 earthquake between Elgin and Lugoff in South Carolina (Figure 1), a region with relatively low background seismicity. Up to April 2024, 97 microearthquakes have been located in this region, with the largest magnitude of 3.6 occurring on June 29, 2022. Like some intraplate earthquakes on the east coast, these earthquakes occurred along the EPFS, a Late Paleozoic dextral strike-slip fault. In a broader sense, several recent moderate-size events, such as the 2011 magnitude 5.8 Mineral, Virginia earthquake (Meng et al., 2018), and the 2020 magnitude 5.2 Sparta, North Carolina earthquake (Figueiredo et al., 2022; Neves et al., 2024), also occurred in the surrounding region of the EPFS. However, on closer examination, most events in the Elgin-Lugoff swarm appeared to occur in a diffuse zone at a high angle to the known faults rather than along the EPFS itself (Howard et al., 2022). Despite the intriguing nature of the swarm sequence, interpreting the tectonic structures hosting this sequence is challenging due to the small magnitudes of the events, the relatively sparse seismic network, and the poorly defined local seismic structure. Additionally, the interpretation may be affected by a potential bias in the cataloged event locations arising from a generic seismic velocity model used in this region. Unlike Charleston, which lies on the Coastal Plain, the Elgin swarm resides on Piedmont and thus represents significantly different geology and seismic structures.

Although the Elgin swarm has not caused significant damage or injuries, it serves as a reminder that earthquakes can occur in unexpected places. Unlike regions such as the Summerville/Charleston area of South Carolina, where historically large earthquakes have occurred in the past, or near Lake Monticello with ongoing swarm-like activities, residents in the Elgin-Lugoff region were unfamiliar with earthquake shaking. This swarm sequence hence provides a rare window of opportunity to study the physical mechanisms of swarms in intraplate regions. It also offers a unique teachable moment to raise earthquake awareness in this region.

In October 2022, 86 SmartSolo nodes (Figure 1) were deployed in Elgin, South Carolina, to record the swarm sequence (Peng et al., 2023). This passive source experiment aims to address several critical questions: What is causing this swarm in an otherwise tectonically quiet region? Is the zone of seismicity as diffuse as it appears, and what is the state of seismic stress in Elgin? In this study, we present the network geometry, and observations of waveforms and other metrics in comparison with nearby broadband recordings. In addition, we apply a combination of machine learning phase picking method and a matched filter method (Neves et al., 2024) to enhance the event detection using up to 4 months of continuous waveform data. We also determine the magnitudes of newly detected events and relocate them with double difference method to obtain a high-resolution catalog during this period. This experiment seeks to improve the spatial and temporal resolution of the swarm, enabling a deeper understanding of its origins.

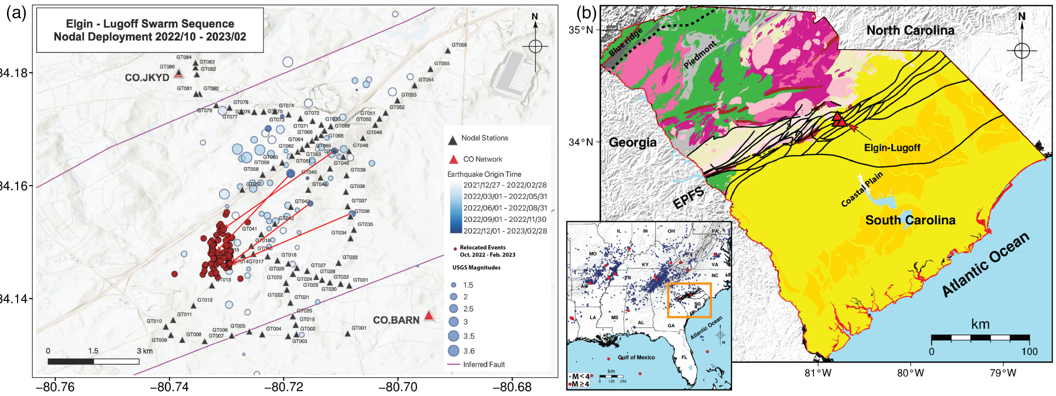

Figure 1. Spatial distribution of the 86 SmartSolo nodes, two SCSN stations, and ∼ 85 swarm events recorded USGS from December 27, 2021 to January 20, 2023. Relocated events, marked by brown circles, are discussed further in later sections. The left map shows the South Carolina geology map (Horton et al., 2017) with the NE-SW structural features of the EPFS in black. Inset map highlights the study region in red and shows seismicity in the southeastern United States over the last 20 years.

2 Data and Methods

2.1 Instrument Deployment and Data Quality

Each node had a 15-day internal battery and was connected to a ∼100-day external battery pack, allowing them to record continuously for up to 4 months. Such a long duration was extremely valuable since the seismicity rate of the swarm sequence had already decreased by the time of the deployment. The instrument gain was set to 24 dB and the sampling rate was 250 Hz. In addition to the 86 nodes, South Carolina Seismic Network (SCSN) staff deployed a broadband seismometer CO.JKYD, co-located with a nodal station GT086. Another strong motion station CO.BARN was previously deployed by the SCSN following the first event in December 2021, just south of the swarm, and has proven to be valuable for recording the subsequent episodes in May and June 2022. Seismic data from both CO.JKYD and CO.BARN can be accessed in real-time from EarthScope Data Management Center (https://ds.iris.edu/mda/CO/). One station GT006 was destroyed by a lawnmower shortly after the initial deployment. The remaining nodal seismic stations were retrieved in early February 2023. The total volume of data recovered was about 2 Terabytes.

Figure 2a shows a comparison of waveforms of a magnitude 2.5 event on October 31, 2022 recorded by two nodal stations (GT001 and GT086), two local stations (CO.JKYD and CO.BARN) and by three regional stations. A zoom-in plot of all nodal-station recording shows clear P and S arrivals and possible changes in the relative amplitudes between P and S waves, which can be used to constrain their focal mechanisms (Fig. 2b). As expected, the waveforms from the GT086 and JKYD stations match very well, after we manually flip the polarity of the nodal station recording (Figure 2c). The reason for such a polarity flip is that for nodal recordings, its positive is downward, rather than upwards as in most broadband recordings. As per manufacturer specification, this polarity flip is not present at frequencies below 1-Hz, due to the instrument response of the nodal geophones. In addition, their normalized spectra for this event also match well (Figure 2d), except that the spectrum of the nodal recording goes to 125 Hz, since the nodal data is recorded at 250 sample/s. We noticed that portion of the nodal recordings clipped slightly (Figure 2c), likely because the event was relatively shallow, and the gain of the nodal recording was set as 24, the highest value for the nodal sensor recordings. Nonetheless, this demonstrates the similarity between these nodes and the broadband recordings when resolving small earthquakes and shows the quality of this data. We also compared background noise levels using probabilistic power spectral density (PPSD) analysis (Peterson et al., 1993) of signals recorded by our Smart-solo 3C nodal sensors against reference data from JKYD. For our study, the computation of PPSD was carried out for one-month data. The PPSD of background noise recorded at JKYD and the colocated nodal station GT086 (Figure 3) indicate that the frequency response of the noise is consistent with the broadband station down to 0.1 Hz.

2.2 1D Velocity Structure Inversion

To construct the 1D velocity model, we used a combination of historical seismicity in the South-Eastern US observed at the CO South Carolina nwtwork and events from during the swarm recorded at both the CO network and the nodal array. For the historical seismicity, we used the USGS reported pick times while for the swarm events we manually re-picked the data to identify the P- and S-wave arrival times. Overall, we used 89 events from the swarm.

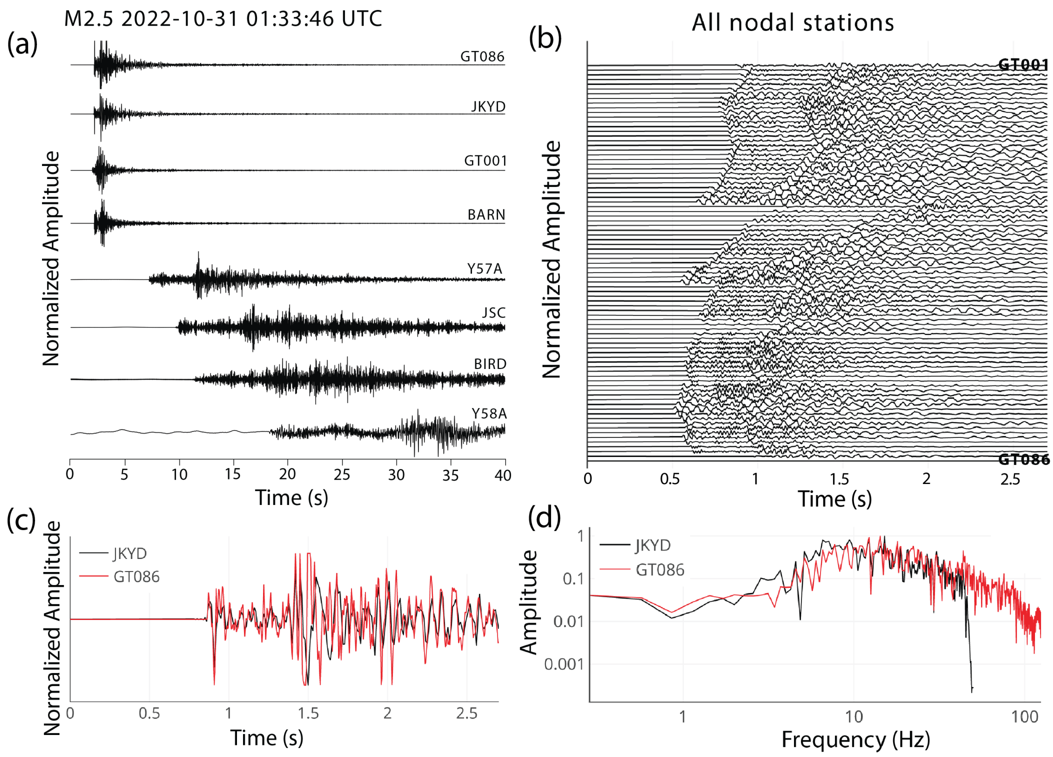

Figure 2. (a) Seismograms comparing recordings between nodal stations and regional stations. (b) Waveform recordings at all nodal stations. (c) Normalized vertical component waveforms recorded at GT086 and co-located JKYD after flipping the polarity of the nodal data. (c) Normalized spectra for the vertical components.

We inverted for the 1-D velocity structure using VELEST (Kissling et al., 1994). As our initial model we used that of Charleston, South Carolina, which has 9 velocity layers including a 700 m upper sediment layer. We fixed the Vp/Vs ratio to 1.73 and varied the interface depths manually, while allowing the inversion to fit the velocities. Acknowledging that the historical seismicity generally included earthquakes are greater distances from the stations while the swarm events included earthquakes only at shorter distances, we first inverted for the upper 3 layers of the model using the swarm events alone, then fixed these layers and inverted for the deeper structure using the historical seismicity. The initial and final 1-D velocity model can be found in Table S1 & S2. As expected, we find that the data are best fit by a velocity model with a thinner sediment layer than the initial Charleston model.

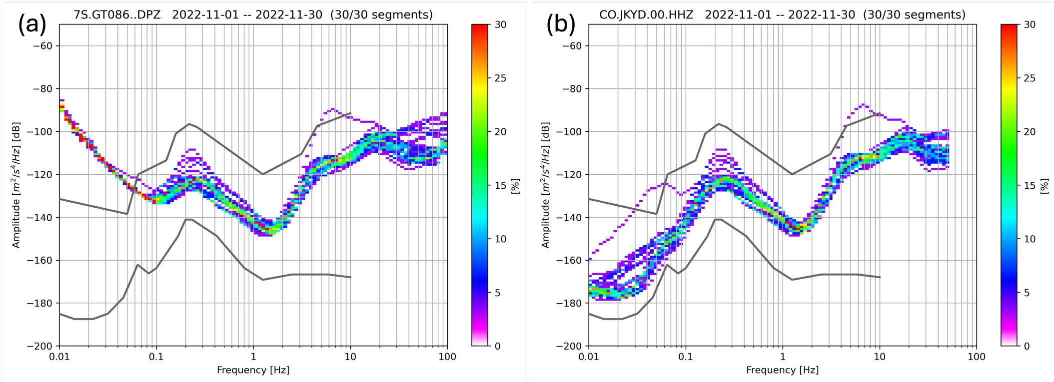

Figure 3. (a) The probabilistic power spectral density (PPSD) of background noise recorded at the (a) broadband seismometer CO.JKYD and (b) GT086. The low and high noise models from (Peterson et al., 1993) are shown as gray curves for reference.

2.3 Event Detection & Location

In this study, we followed the steps outlined in Neves et al. (2024) to perform earthquake detection and relocation. First, we picked P and S arrivals from continuous waveforms with the EQtransformer deep learning model (Mousavi et al., 2020), which has been pre-trained on the STanford Earthquake Dataset (STEAD) (Mousavi et al., 2019) within the Seisbench (Woollam et al., 2022) deep learning toolbox. EQtransformer generates three key predictions: the probability of event detection and the arrival times of P and S waves within a specific period. The results in picked P and S phases, as well as the seismic detection window (Figure 4a), were afterward confirmed and associated as events by establishing a maximum difference of 0.7s in P-wave arrival times between stations and a minimum detection requirement across seven stations.

Thereafter, at the nodal stations, we utilized a MFT to detect additional events, employing those identified through the deep learning approach and existing 4 events as templates. In this process, both templates and continuous waveforms were bandpass filtered within the 1-60 Hz range and downsampled to 120 samples/s. Following this, template waveforms were windowed at 2.5s around the local events, 0.3s before and 2.2s after the event origin time. We applied the mean absolute deviation (MAD) detection thresholds of 14 and a mean cross-correlation threshold of 0.2 (Figure 4b & c). A correlation of the maximum peak amplitude of the vertical component and known local magnitudes for the templates was applied to estimate the local magnitudes for a few template events where the magnitudes are unknown. Finally, detection local magnitudes were computed by comparing their

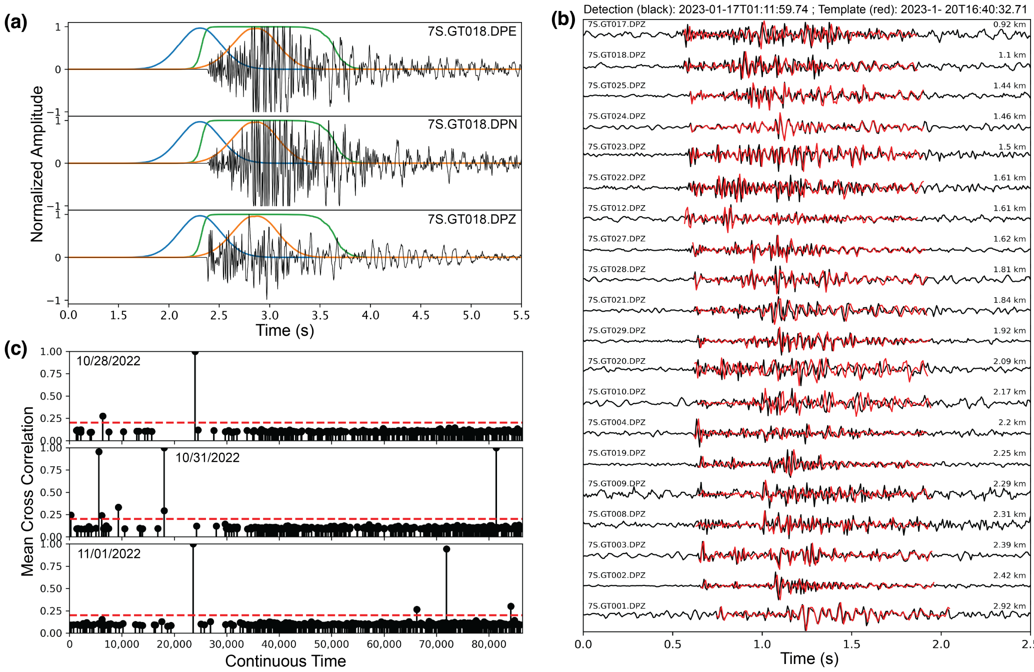

Figure 4. (a) Detection of seismic phase and event using EQTransformer, pre-trained on the STEAD dataset and applied with Seisbench at station GT078 for an M2.5 earthquake occurring on October 31, 2022 (Mousavi et al., 2019, 2020; Woollam et al., 2022). The blue gaussian curve indicates the P-wave arrival, the orange gaussian curve signifies the S-wave arrival, and the green box shape signifies the event detected. (b) Comparison between the continuous waveforms (black) and template waveforms (red) within the 1-60Hz range, demonstrating the detection of an event using template matching technique with a mean CC value of 0.77 and MAD value of 79.2. (c) Examples of daily detections from 28 October to 1 November 2022. The dashed line on each plot represents the detection threshold defined by a $MAD \geq 14$ and mean CC value ≥ 0.2.

peak amplitudes with those of the template events, assuming that an amplitude of 10 is proportional to an increase in magnitude relative to the template magnitude (Peng & Zhao, 2009).

Once all events within our specified nodal deployment timeframe had been detected, event phase information directly from initial absolute location using HYPOINVERSE-2000 (Klien, 2002) was used to derive the catalog differential times for hypoDD (Waldhauser, 2001), setting a limit of 4 maximum neighboring events and a search radius of 5 km. For waveform cross-correlation differential times, we employed EQCorrscan (Chamberlain et al., 2018), designed to detect and analyze repeating or nearly repeating seismic events. Here, we extracted 0.3 seconds around the P & S arrival on both the vertical and horizontal components. This included 0.1 seconds before the arrival and 0.2 seconds after the arrival, with a shift length of 0.05 seconds. Such a short time window was used to ensure that the correlated arrivals were from similar phases, eliminating interference from different seismic phases. We cross-correlated every event pair in a 3 km radius, and each event pair must have at least 3 differential time measurements. The inversion technique used to invert the event locations is the conjugate gradients method, specifically the LSQR (Paige & Saunders, 1982).

2.4 Focal Mechanism Solution

To obtain the focal mechanism solutions, we manually picked the first motion polarity measurements on the vertical components and flipped these polarities on the processed waveforms due to the aforementioned polarity flip caused by the instrument response. Following this, we measured the peak amplitudes of the P and S waves by calculating and then summing the difference between the maximum and minimum amplitude values over all three channels of the seismograms using a window of -0.01 to 0.5 seconds around the seismic phase arrival. Noise amplitudes were similarly computed using a window of -0.5 to -0.02 seconds before the P-wave arrivals. Then we determined the take-off angles by integrating our regional crustal velocity model (Table S1) and ak135-f (Kennett B. L. & R., 1995) for deeper structures. For focal mechanism inversion, we used the HASH program (Hardebeck & Shearer, 2002), which takes the polarities, signal amplitude ratios, and take-off angles as input. The criteria set for the HASH algorithm during the moment tensor inversion includes a minimum of 15 polarity observations, a signal-to-noise amplitude ratio not less than 2.0, and a grid search of 15° increments for the strike, dip, and rake to find the set of acceptable focal mechanisms, permitting up to a 20% error in polarity measurements.

3 Results

3.1 Expanding Seismic Catalog through Nodal Station Detections

Using only 4 events recorded by USGS throughout the nodal deployment for templates, we detected 26 new local events in the magnitude range of -0.56 to 1.06 using the single station MFT on the broadband JKYD station. Following this, combining EQTransformer model with existing MFT methodology, we expanded the nodal station detection to a total of 100 microearthquakes (Figure 5a, Table S4). The largest event occurred on October 31, 2022, with a M2.54 and was listed in the USGS catalog. Additionally, the majority of the newly detected events within the swarm display significantly lower magnitudes (M-2.17 to M2.54) than those reported by the USGS during the nodal period and over the entire observational period of the swarm (Figure 5a).

According to the Gutenberg-Richter (GR) law (Gutenberg, 1944), earthquake magnitudes within a given area follow an exponential distribution, presented by the relation, $\log_{10} N(m) = a - bm$. Here, $N(m)$ represents the count of earthquakes with magnitudes greater or equal to m, and a and b are fixed constants. By using the Maximum Curvature method (Wiemer & Wyss, 2000) with a bin width of 0.1 magnitude, we estimated the earthquake's magnitude of completeness (M_c) of the nodal deployment as -0.22 and the USGS recorded events over the entire duration of the swarm as 2.30 (Figure 5b). Furthermore using maximum likelihood estimation (Aki, 1965), we determined the b-value as 0.68 and 0.85 respectively. Our analysis indicates a significant presence of small-magnitude events in the swarm area, suggesting that further investigations are necessary both before and after the nodal deployment to fully understand the dynamics of the swarm sequence.

3.2 Seismicity Location and Space-Time Evolution

Using the double-difference technique hypoDD, we obtained and refined the spatial distribution of the 100 swarm events identified during the nodal period. Compared to a broader swarm area reported in the USGS catalog for the entire swarm duration, our analysis revealed a more confined seismogenic zone, prominently showing a single and distinct cluster zone (Figure 6a&b). The high-resolution and localized swarm zone is likely a result of the benefit of deploying densely spaced seismic nodal stations within the Elgin vicinity, unlike the broader network of regional stations that were used to locate events recorded by the USGS throughout the swarm. Specifically, this cluster reflects a nearly north-south trending and steeply west-dipping seismically active structure (Figure 6c & 7a), consistent with one of the magnetic anomalies in the EPFS (Shah et al., 2023). Predominantly, the relocated swarm activities concentrate at shallow depths between 1.5 to 3.5 km.

Focal mechanism analysis indicates a prevalence of right-lateral strike-slip with minor thrust components (Figure 6b & 7a, Table S3). Drawing inference that the swarm is likely influenced by fluid migration within localized subsurface weak zones suggested by the two

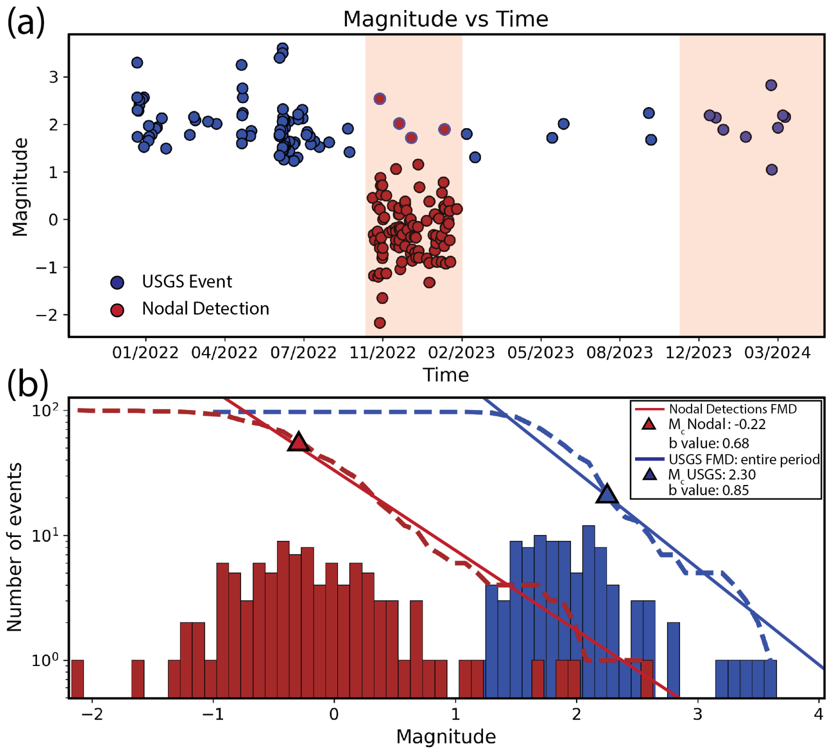

Figure 5. (a) Magnitudes against time for the nodal period and entire USGS catalog. Brown circles with blue border are events detected by both the nodal stations and recorded by USGS during the nodal period in red. (b) GR distribution of the Elgin swarm sequence. The discrete and cumulative number of events versus magnitude are shown in brown and blue respectively.

distinct seismicity patterns in (Figure 7b), we explored the possibility of identifying a migration pattern indicative of fluid diffusion (Shapiro et al., 1997). Therefore, we determined the triggering front r(t) $= \sqrt{4\pi Dt}$, where t denotes the time since injection began and D is fluid hydraulic diffusivity, assuming that the fluid-saturated medium is uniform and isotropic having a specific point source, which influences the variation in pore pressure (Figure 7c). The computed fluid hydraulic diffusivity using event locations relative to the first detected event of M0.45 recorded on October 21, 2022 at 22:21:25.0 is $0.03\,\mathrm{m}^2/\mathrm{s}$. This aligns with the expected diffusivity range ($0.01 - 10\,\mathrm{m}^2/\mathrm{s}$) for swarms in other regions (Minetto et al., 2022).

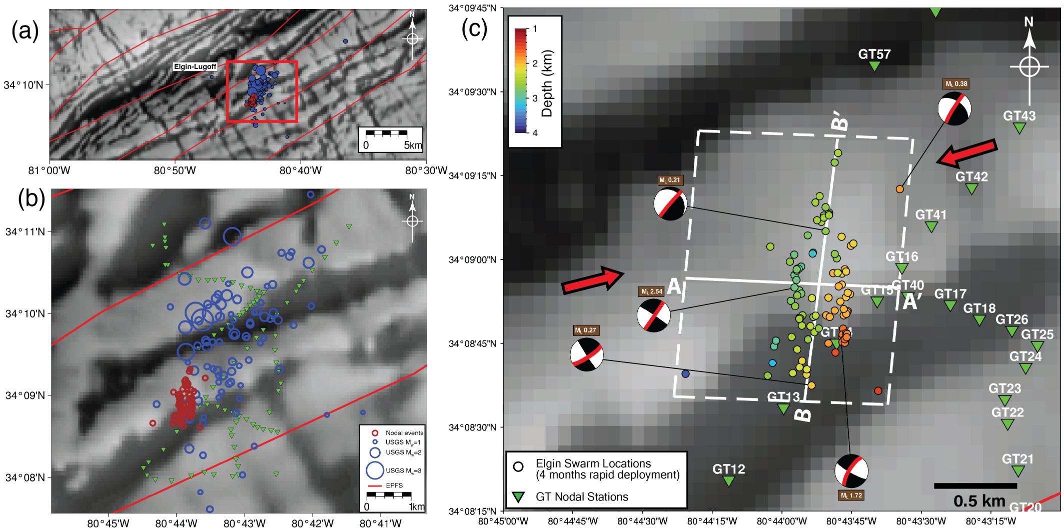

Figure 6. (a) Zoomed-out section of the magnetic lineaments within the EPFS highlighting the general fault trends and the placement of swarms within the fault context (Shah et al., 2023). (b) Relocated events identified by the nodal stations extends beyond a magnetic lineament structures. (c) Relocated swarm events are color-coded by depth, with brown beach balls indicating focal mechanisms and their magnitudes. Preferred nodal planes on focal mechanism solution is highlighted in red. Red arrows depict the maximum principal stress direction.

4 Discussion & Conclusion

These initial findings present enhanced detection and relocation techniques, increasing seismic detection by 25 times over four months. The enhanced catalog for the nodal period predominantly contains smaller magnitude events, with a M_c of -0.22, compared to a M_c of 2.30 of events recorded by the USGS for the entire swarm period (Figure 5b, Table S5). While the Gutenberg-Richter law provides an initial assessment of the frequency-magnitude distribution and parameters such as b-value and M_c, we refrain from heavily relying on it pending a comprehensive detection analysis throughout the entire swarm's duration. The relocated swarm sequence reveals a clear north-south striking and west-dipping strike-slip fault structure that hosts the swarm sequence within a confined single cluster, aligning conjugate with EPFS fault trend (Hatcher et al., 1977) (Figure 6a). This orientation may be favorable for reactivation as they are at an angle to the horizontally oriented ENE-WSW principal stress direction in the southeastern United States (Levandowski et al., 2018) (Figure 6c). Although the relocated swarm is shifted to the right and is not spatially within the nodal network. We will expand nodal station coverage, incorporate CO regional stations, and utilize the relocated events to improve the inversion of the shallow velocity structures, thereby providing robust constraint to the swarm locations.

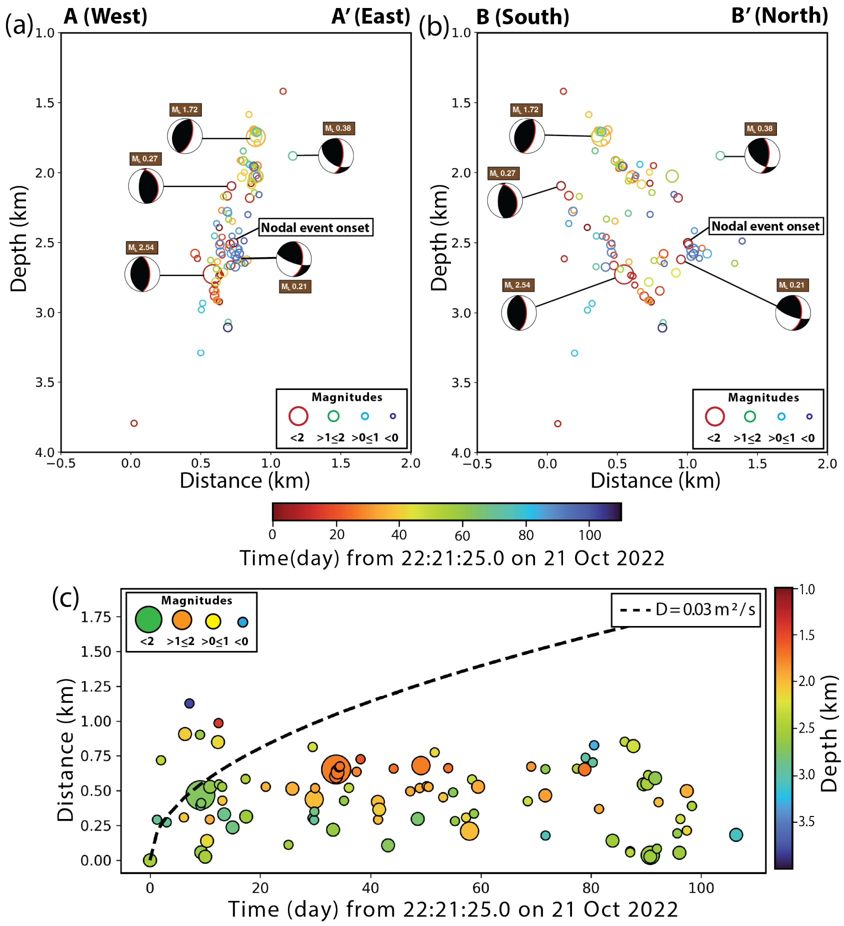

Figure 7. Cross-sectional view of the swarm events and focal mechanisms shown in (Figure 6c) illustrating a structurally west dipping seismic zone. (a) Depth and Temporal Cross-section along the longitudinal axis (A - A') and (b) latitudinal axis (B - B'). (c) Swarm migration over a short-time period modeled with hydraulic diffusivity (D).

This provides a first assessment of the Elgin Swarm and highlight the importance of subsequent efforts focusing on developing a comprehensive catalog for the entire swarm duration combining seismic data from the nodal stations and regional stations from the CO network. Such a catalog will enhance our understanding of the fault's extent and contribute to elucidating the propagation direction and space-time migration, which were not observed during the nodal period since any potential migration patterns are typically detected at the swarm onset. Subsequent research should consider building on these findings by monitoring hydroseismicity not fully captured by the relocated swarm (Figure 7c) and exploring the influence of water on fault planes (Shelly et al., 2013). Considering the proximity of the Wateree River, fluctuating river discharges and seasonal precipitation may be contributing to the current seismicity (Howard et al., 2022).

In addition, a resurgence of the swarm sequence has been observed since mid-October 2023 featuring notable seismic events with duration magnitudes of M_d 2.2 and M_d 2.1 on 22 December 2023 at 08:16:43 UTC and 30 December 2023 at 10:27:41 UTC. In response to this activity, we initiated a further deployment from October 2023 involving twenty stations to cover up a wider spatial area (Figure S1) and continue monitoring seismic activity within the Elgin-Lugoff region for six months. This expanded data recording and increased area of coverage will contribute to an increase in the number of detections, more precise relocations, and the development of robust and accurate focal mechanisms

5 Data Availabilty Statement

The 4 months ∼2Tb continuous waveforms used for this study will be accessible through the EarthScope Consortium PH5 Web Services (https://service.iris.edu) under the 7S (2022-2023) network (Peng & Frost, 2022).

6 Acknowledgement

We appreciate Dr. Scott Howard's assistance with the nodal station deployment and his contribution that improved the manuscript. We also thank Dr. Anjana Shah for providing the regional magnetic field anomaly map and express our gratitude to the students from Georgia Institute of Technology, School of Earth and Atmospheric Sciences and the University of South Carolina, School of Earth, Ocean, and Environment for their significant support during the deployment. Additionally, we thank the Society of Exploration Geophysics' student chapter outreach grant for providing additional financial support to our fieldwork. This work was funded by the National Science Foundation EAR-Geophysics grants (EAR-2322461 and EAR-2321094 to OEA, LYC, MN and ZP, and EAR-2303140 and EAR-2321095 to DF).

References

Aki, K. (1965). Maximum likelihood estimate of b in the formula log n= a-bm and its confidence limits. *Bull. Earthquake Res. Inst., Tokyo Univ.*, *43*, 237–239.

Benoit, J. P., & McNutt, S. R. (1996). Global volcanic earthquake swarm database and preliminary analysis of volcanic earthquake swarm duration. *Annals of Geophysics*, *39*(2).

Chamberlain, C. J., Hopp, C. J., Boese, C. M., Warren-Smith, E., Chambers, D., Chu, S. X., ... Townend, J. (2018). Eqcorrscan: Repeating and near-repeating earthquake detection and analysis in python. *Seismological Research Letters*, *89*(1), 173–181.

Chen, X., Shearer, P., & Abercrombie, R. (2012). Spatial migration of earthquakes within seismic clusters in southern california: Evidence for fluid diffusion. *Journal of Geophysical Research: Solid Earth*, *117*(B4).

Figueiredo, P., Hill, J., Merschat, A., Scheip, C., Stewart, K., Owen, L., ... others (2022). The mw 5.1, 9 august 2020, sparta earthquake, north carolina: The first documented seismic surface rupture in the eastern united states. *GSA Today*, *32*(3-4).

Fischer, T., Horálek, J., Hrubcová, P., Vavryčuk, V., Bräuer, K., & Kämpf, H. (2014). Intra-continental earthquake swarms in west-bohemia and vogtland: a review. *Tectonophysics*, *611*, 1–27.

Gutenberg, C. F. R., B. (1944). Frequency of earthquakes in california. *Bull. Seismol. Soc. Am. 34*, 185–188. doi: 10.1785/bssa0340040185

Hardebeck, J. L., & Shearer, P. (2002). A new method for determining first-motion focal mechanisms. *Bull. Seismol. Soc. Am.*(no. 6), 2264–2276. doi: 10.1785/0120010200

Hatcher, J., Robert D., Howell, D. E., & Talwani, P. (1977, oct). Eastern piedmont fault system: Speculations on its extent. *Geology*, *5*(10), 636. doi: 10.1130/0091-7613(1977)5⟨636:EPFSSO⟩2.0.CO;2

Hill, D. P. (1977). A model for earthquake swarms. *Journal of Geophysical Research*, *82*(8), 1347–1352.

Holtkamp, S., & Brudzinski, M. R. (2014). Megathrust earthquake swarms indicate frictional changes which delimit large earthquake ruptures. *Earth and Planetary Science Letters*, *390*, 234–243.

Horton, J. D., San Juan, C. A., & Stoeser, D. B. (2017). *The state geologic map compilation (sgmc) geodatabase of the conterminous united states* (Tech. Rep.). US Geological Survey.

Howard, C. S., Jaume, S., White, S. M., & Talwani, P. (2022). *Report on elgin-area earth-*

quakes. Retrieved from https://www.dnr.sc.gov/geology/pdfs/EarthquakeReport-ElginArea2022.pdf

Kennett B. L., E. E. R., & R., B. (1995). Constraints on seismic velocities in the earth from travel times. *Geophys. J. Int.*, 108-124.

Kissling, E., Ellsworth, W., Eberhart-Phillips, D., & Kradolfer, U. (1994). Initial reference models in local earthquake tomography. *Journal of Geophysical Research: Solid Earth*, *99*(B10), 19635–19646.

Klien, F. (2002). User's guide to hypoinverse-2000, a fortran program to solve for earthquake locations and magnitudes. , 123. Retrieved from https://pubs.usgs.gov/publication/ofr02171 doi: 10.3133/ofr02171

Levandowski, W., Herrmann, R. B., Briggs, R., Boyd, O., & Gold, R. (2018). An updated stress map of the continental united states reveals heterogeneous intraplate stress. *Nature Geoscience*, *11*(6), 433–437.

Lohman, R. B., & McGuire, J. J. (2007). Earthquake swarms driven by aseismic creep in the salton trough, california. *Journal of Geophysical Research: Solid Earth*, *112*(B4).

Meng, X., Yang, H., & Peng, Z. (2018). Foreshocks, b value map, and aftershock triggering for the 2011 mw 5.7 virginia earthquake. *Journal of Geophysical Research: Solid Earth*, *123*(6), 5082-5098. Retrieved from https://agupubs.onlinelibrary.wiley.com/doi/abs/10.1029/2017JB015136 doi: https://doi.org/10.1029/2017JB015136

Minetto, R., Helmstetter, A., Schwartz, S., Langlais, M., Nomade, J., & Guéguen, P. (2022). Analysis of the spatiotemporal evolution of the maurienne swarm (french alps) based on earthquake clustering. *Earth and Space Science*, *9*(7), e2021EA002097.

Mogi, K. (1963). Some discussions on aftershocks, foreshocks and earthquake swarms-the fracture of a semi finite body caused by an inner stress origin and its relation to the earthquake phenomena. *Bull. Earthq. Res. Inst.*, *41*, 615–658.

Mousavi, S. M., Ellsworth, W. L., Zhu, W., Chuang, L. Y., & Beroza, G. C. (2020, 08). Earthquake transformer—an attentive deep-learning model for simultaneous earthquake detection and phase picking. *Nature Communications*, *11*(1), 3952. Retrieved from https://doi.org/10.1038/s41467-020-17591-w doi: 10.1038/s41467-020-17591-w

Mousavi, S. M., Sheng, Y., Zhu, W., & Beroza, G. C. (2019). Stanford earthquake dataset (stead): A global data set of seismic signals for ai. *IEEE Access*. doi: 10.1109/ACCESS.2019.2947848

Neves, M., Chuang, L. Y., Li, W., Peng, Z., Figueiredo, P. M., & Ni, S. (2024). Complex rupture dynamics of the extremely shallow august 2020 m5. 1 sparta, north carolina earthquake. *Communications Earth & Environment*, *5*(1), 163.

Paige, C. C., & Saunders, M. A. (1982, mar). Lsqr: An algorithm for sparse linear equations and sparse least squares. *ACM Trans. Math. Softw.*, *8*(1), 43–71. Retrieved from https://doi.org/10.1145/355984.355989 doi: 10.1145/355984.355989

Peng, Z., Chuang, L., Mach, P., Frost, D., Howard, S., & White, S. (2023, April). High-resolution imaging of the elgin-lugoff earthquake swarm sequence in south carolina using a dense seismic nodal array. In *Annual meeting of the seismological society of america.* Springer.

Peng, Z., & Frost, D. (2022). *Nodal deployment for the elgin-lugoff south carolina earthquake swarm.* IRIS DMC. Retrieved from https://www.fdsn.org/networks/detail/7S_2022/ doi: 10.7914/CGYQ-NK68

Peng, Z., & Zhao, P. (2009). Migration of early aftershocks following the 2004 parkfield earthquake. *Nature Geoscience*, *2*(12), 877–881.

Peterson, J., et al. (1993). *Observations and modeling of seismic background noise* (Vol. 93). US Geological Survey Reston, VA, USA.

Ross, Z. E., Cochran, E. S., Trugman, D. T., & Smith, J. D. (2020). 3d fault architecture controls the dynamism of earthquake swarms. *Science*, *368*(6497), 1357–1361.

Ross, Z. E., Trugman, D. T., Hauksson, E., & Shearer, P. M. (2019). Searching for hidden earthquakes in southern california. *Science*, *364*(6442), 767–771.

Shah, A. K., Pratt, T. L., & Horton, J. J. (2023). Rift basins and intraplate earthquakes: New high-resolution aeromagnetic data provide insights into buried structures of the charleston, south carolina seismic zone. , *24*. doi: https://doi.org/10.1029/2022GC010803

Shapiro, S. A., Huenges, E., & Borm, G. (1997). Estimating the crust permeability from fluid-injection-induced seismic emission at the ktb site. *Geophysical Journal International*, *131*(2), F15–F18.

Shelly, D. R., Ellsworth, W. L., & Hill, D. P. (2016). Fluid-faulting evolution in high definition: Connecting fault structure and frequency-magnitude variations during the 2014 long valley caldera, california, earthquake swarm. *Journal of Geophysical Research: Solid Earth*, *121*(3), 1776–1795.

Shelly, D. R., Hill, D. P., Massin, F., Farrell, J., Smith, R. B., & Taira, T. (2013). A fluid-driven earthquake swarm on the margin of the yellowstone caldera. *J. Geophys.*

Res. Solid Earth, *118*, 4872–4886. doi: 10.1002/jgrb.50362

Toda, S., Stein, R. S., & Sagiya, T. (2002). Evidence from the ad 2000 izu islands earthquake swarm that stressing rate governs seismicity. *Nature*, *419*(6902), 58–61.

Waldhauser, F. (2001). hypodd-a program to compute double-difference hypocenter locations. *USGS Publications Warehouse*. Retrieved from https://pubs.usgs.gov/publication/ofr01113 doi: 10.3133/ofr01113

Wiemer, S., & Wyss, M. (2000). Minimum magnitude of completeness in earthquake catalogs: Examples from alaska, the western united states, and japan. *Bulletin of the Seismological Society of America*, *90*(4), 859–869.

Woollam, J., Münchmeyer, J., Tilmann, F., Rietbrock, A., & Lange, D. (2022, 03). Seisbench — a toolbox for machine learning in seismology. *Seismologial Research Letters*, *93*, 1695–1709. Retrieved from https://doi.org/10.1785/0220210324 doi: 10.1785/0220210324

Supporting Information for "Localized west-dipping seismic structure defines the Elgin-Lugoff Swarm Sequence in South Carolina"

Oluwaseyifunmi E. Adeboboye[1], Lindsay Y. Chuang[1], Miguel Neves[1,2], Zhigang Peng[1], Dan Frost[3], Steve Jaume'[4]

[1]School of Earth and Atmospheric Sciences, Georgia Institute of Technology, USA
[2]Université Côte d'Azur, IRD, CNRS, OCA, Géoazur, Sophia Antipolis, France
[3]School of the Earth, Ocean, and the Environment College of Arts and Sciences, University of South Carolina, USA
[4]Department of Geology and Environmental Sciences, College of Charleston, USA

Contents of this file

1 Introduction

This supporting information includes an additional figure and table that complement our study. We present the initial and final inverted velocity models (Table S1 & S2) used for the relocation of the swarms, along with the locations of our ongoing six-month deployment configuration (Figure S1), which aims to cover a broader spatial extent and will be valuable for future analysis of the swarms. Additionally, an animated GIF image depicting the swarm migration over time and the identified structures in 3D will be uploaded separately as part of the supplementary material. We also provide results from our Match Filter Detection, the relocated catalog, and the inverted focal mechanisms.

2 Initial and Final Inverted Velocity Model

Table S1. Initial velocity model

Depth (km)	V_p (km/s)	V_s (km/s)
0.00	2.20	0.75
0.70	5.50	3.22
1.50	5.60	3.27
3.00	5.75	3.36
7.00	5.90	3.45
10.00	6.45	3.77
20.00	6.70	3.92
32.00	8.15	4.77

[a]Initial Charleston 1-D velocity model.

Table S2. Initial velocity model

Depth (km)	V_p (km/s)	V_s (km/s)
0.00	5.45	2.72
1.50	6.08	2.72
3.00	6.08	3.55
7.00	6.23	3.55
10.00	6.23	3.60
20.00	6.42	3.61
22.00	6.47	3.61
30.00	7.16	3.61
40.00	8.16	4.71

[a]Initial Charleston 1-D velocity model.

3 Current Ongoing Nodal Deployment Status in the Elgin-Lugoff Area

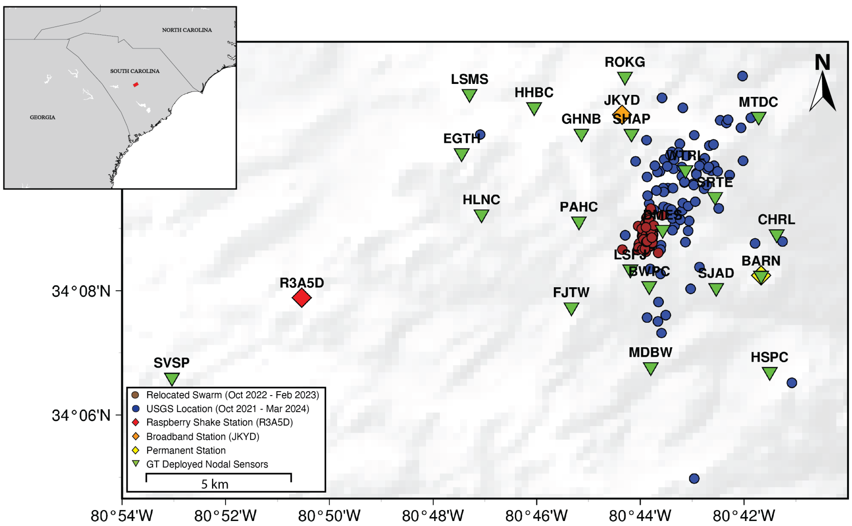

Figure S1. The current locations of seismic nodal deployments from March 19, 2024, aimed at enhancing the monitoring of the earthquake swarm sequence. Among these, six sensors (LSMS, EGTH, PAHC, LSFJ, BWPC, and SJAD) have been in operation since October 2023. The red rectangle in the blow-out map depicts the deployment area.